

Non-equilibrium carrier dynamics and band structure of graphene on 2D tin

Maria-Elisabeth Federl,¹ Niklas Witt,^{2,3} Biao Yang,⁴ Niklas Hofmann,⁵ Johannes Gradl,⁵ Leonard Weigl,⁵ Ignacio Piquero-Zulaica,⁴ Johannes V. Barth,⁴ Neeraj Mishra,^{6,7} Camilla Coletti,^{6,7} Tim O. Wehling,^{8,9} and Isabella Gierz^{5,*}

¹*Department for Experimental and Applied Physics,
University of Regensburg, 93053 Regensburg, Germany*

²*I. Institute of Theoretical Physics,
University of Hamburg, 22607 Hamburg, Germany*

³*The Hamburg Centre for Ultrafast Imaging, 22761 Hamburg, Germany*

⁴*Physics Department E20, TUM School of Natural Sciences,
Technical University of Munich, 85748 Garching, Germany*

⁵*Department for Experimental and Applied Physics,
University of Regensburg, Regensburg, Germany*

⁶*Center for Nanotechnology Innovation@NEST,
Istituto Italiano di Tecnologia, Pisa, Italy*

⁷*Graphene Labs, Istituto Italiano di Tecnologia, Genova, Italy*

⁸*I. Institute of Theoretical Physics, University of Hamburg,
Notkestrasse 9, 22607 Hamburg, Germany*

⁹*The Hamburg Centre for Ultrafast Imaging,
Luruper Chaussee 149, 22761 Hamburg, Germany*

(Dated: May 3, 2024)

Abstract

Intercalation of epitaxial graphene on SiC(0001) with Sn results in a well-ordered 2D metallic Sn phase with a (1×1) structure at the interface between SiC substrate and quasi-freestanding graphene. The 2D Sn phase exhibits exotic electronic properties with Dirac-like and flat bands coexisting close to the Fermi level that exhibit both Zeeman- and Rashba-type spin splittings. Possible inter-layer interactions between the 2D Sn layer and graphene that may result in emerging electronic properties remain unexplored. We use time- and angle-resolved photoemission spectroscopy to reveal a surprisingly short-lived non-equilibrium carrier distribution inside the Dirac cone of graphene. Further, we find that the graphene π -band exhibits a transient down-shift that we attribute to charging of the graphene layer with holes. We interpret our results with support from density functional theory calculations of the graphene - 2D Sn heterostructure that reveal a substantial hybridization between graphene π -band and Sn p_z -states that opens up a ~ 230 meV band gap inside the Dirac cone and delocalizes the charge carriers over both the graphene and 2D Sn layers. Our results have important implications for the design of future ultrafast optoelectronic devices that may find applications in the fields of light harvesting and detection, as supercapacitors, or in novel quantum computing technologies.

INTRODUCTION

Van der Waals (vdW) heterostructures [1, 2] are novel artificial materials with tailored electronic properties. Common control parameters are the choice of specific materials to be stacked, layer thicknesses and spacings, and the relative orientation of the layers. VdW heterostructures are a possible platform for the experimental realization of various exotic quantum phases [3] and may enable new technologies in the fields of flexible electronics, optoelectronics, spintronics, and quantum computing [4, 5]. They are commonly made by manual cleaving and stacking of layered materials into heterostructures. This procedure works well for proof-of-principle devices. However, sample sizes are small and the interfaces are usually dirty. These problems are resolved by confinement heteroepitaxy [6–8] where various kinds of atoms are intercalated at the interface between epitaxial graphene and SiC substrate in ultra-high vacuum. The intercalated atoms self-assemble into well-ordered 2D surface structures on SiC(0001) with quasi-freestanding graphene on top.

Here, we focus on a heterostructure consisting of graphene and 2D metallic Sn forming a (1×1) structure on SiC(0001). This system has been previously investigated for the following reasons: Sn intercalation can be used for the fabrication of almost charge-neutral graphene [9]. Further, the intercalated Sn forms a triangular lattice with exotic electronic properties where Dirac-like and flat bands coexist close to the Fermi level [10, 11]. Finally, the spin degeneracy of the states at the K-point is lifted due to spin-orbit coupling and broken inversion symmetry resulting in both Zeeman- and Rashba-like spin splittings [11, 12]. Emergent electronic properties that may arise from interlayer interactions between graphene and 2D Sn have received little attention so far. Also, non-equilibrium carrier dynamics that is essential for understanding and optimizing the performance of various devices such as transistors, photodetectors, or solar cells remains largely unexplored.

Here, we combine high-resolution angle-resolved photoemission spectroscopy (ARPES) measurements and density functional theory (DFT) calculations to determine the band structure of 2D Sn on SiC(0001), confirming the formation of the well-known metallic (1×1) structure. Next, we use time-resolved ARPES (trARPES) to explore the non-equilibrium carrier dynamics and transient band structure of graphene on 2D Sn after photoexcitation with visible pump pulses with a photon energy of $\hbar\omega_{pump} = 2 \text{ eV}$. We find surprisingly short-lived population dynamics inside the Dirac cone of graphene with lifetimes below $\sim 400 \text{ fs}$, suggesting carrier relaxation via states of 2D Sn. Further, our trARPES results reveal a transient accumulation of carriers above the Dirac point of graphene, resulting in a non-thermal carrier distribution. We also find a short-lived transient rigid downshift of the graphene π -bands that we attribute to a transient charging of the graphene layer with holes. DFT calculations of the graphene - 2D Sn heterostructure reveal a strong hybridization between the Dirac cone of graphene and the flat bands consisting of Sn p_z orbitals. The corresponding wave functions are delocalized over both the graphene and the 2D Sn layer and might mediate ultrafast charge transfer between the layers.

Our results provide the fundamental understanding of ultrafast carrier dynamics in graphene/ (1×1) Sn/SiC(0001) relevant for the development of faster and more efficient optoelectronic devices.

METHODS

A carbon buffer layer with $(6\sqrt{3} \times 6\sqrt{3})R30^\circ$ structure was grown by thermal decomposition of hydrogen-etched SiC(0001) in Ar atmosphere [13]. Sn was then deposited from a commercial Knudsen cell at room temperature and intercalated by postannealing at 900°C for 5 minutes.

High-resolution ARPES experiments were performed at the 1^2 -ARPES end station at Bessy-II [14] with a photon energy of $\hbar\omega = 150\text{ eV}$ at a sample temperature of $T = 13.4\text{ K}$. Energy and angular resolution were $\sim 160\text{ meV}$ and $\sim 0.5^\circ$, respectively.

The trARPES setup was based on a Ti:Sa amplifier (Astrella, Coherent) with a repetition rate of 1 kHz , a pulse energy of 7 mJ and a pulse duration of 35 fs . 5 mJ of output energy were used to seed an optical parametric amplifier (Topas Twins, Light Conversion) the second harmonic of which was used to generate visible pump pulses with a photon energy of $\hbar\omega_{pump} = 2\text{ eV}$ and a fluence of $F = 0.3\text{ mJ/cm}^2$. The remaining 2 mJ of pulse energy were frequency doubled and used for high harmonics generation in Argon. A single harmonic with a photon energy of $\hbar\omega_{probe} = 21.7\text{ eV}$ was selected with a grating monochromator. These extreme ultraviolet (XUV) probe pulses were used to eject photoelectrons from the sample. The resulting photocurrent was measured with a hemispherical analyzer (Phoibos 100, Specs) as a function of kinetic energy and emission angle, directly yielding snapshots of the occupied part of the transient band structure of the sample. The energy and temporal resolutions were 190 meV and 150 fs , respectively.

We performed the DFT calculations using the Vienna Ab-initio Simulation Package (VASP) [15–17] within the generalized gradient approximation of Perdew, Burke, and Ernzerhof (GGA-PBE) [18] and the projector augmented wave (PAW) [19, 20] basis sets. We obtain the total energy, relaxed structure and electronic structure employing a kinetic energy cutoff of 400 eV and a Γ -centered mesh of $12 \times 12 \times 1$ in our calculations. The conjugate gradient algorithm is used for ionic relaxation until all force components are smaller than 0.005 eV \AA^{-1} . We do not include spin-orbit coupling in our calculations. In all calculations we keep a fixed lattice constant of $a = 3.095\text{ \AA}$ for the SiC bulk and Sn(1×1) phase. For the heterostructure with epitaxial graphene, we adopt a $(\sqrt{3} \times \sqrt{3})R30^\circ$ super cell of the Sn/SiC(0001) surface such that graphene is stretched by approx. 15% with a C-C distance of $d_{C-C} \approx 1.63\text{ \AA}$. We employed a vacuum of around 6 \AA to eliminate spurious interactions

within the periodic cell scheme. The data of our DFT calculations is made available at [21].

RESULTS

In Fig. 1 we present high-resolution ARPES results for the graphene - 2D Sn heterostructure. Figure 1a shows the photocurrent at three selected energies as a function of the two in-plane momenta k_x and k_y . The Brillouin zones of graphene and 2D Sn are indicated by dashed orange and blue lines, respectively. At $E = -0.08$ eV, just below the Fermi level, we observe small dots at the corners of the graphene Brillouin zone originating from the almost charge neutral Dirac cone of graphene. We further find two Sn-related electron pockets labeled S_1 and S_2 , respectively. S_1 is centered around the K-points of the hexagonal Brillouin zone of 2D Sn. S_2 exhibits the shape of a distorted hexagon centered around the Γ -point with corners pointing towards the K-points of 2D Sn. At lower energies ($E = -1.15$ eV and $E = -1.73$ eV) the Dirac cone of graphene exhibits its typical triangular shape. The hexagon with the corners pointing towards the K-points of the Brillouin zone of 2D Sn belongs to another Sn-related state labeled S_3 . The intensity around the Γ -point is attributed to states belonging to the SiC substrate.

The dispersion of the electronic states along the green and red lines in Fig. 1a is shown in Figs. 1b and c, respectively, together with DFT calculations for a Sn (1×1) structure on SiC(0001) (blue lines) and free-standing graphene (orange lines). The calculations were shifted by -290 meV (2D Sn) and $+80$ meV (graphene) to account for the experimentally observed doping level. In addition, the DFT calculations for free-standing graphene were stretched by a factor of 1.18 in energy to account for the experimentally observed Fermi velocity v_F . The overall agreement between theory and experiment, as well as with existing literature [9–12] is excellent and provides direct evidence that the intercalated Sn forms the well-known metallic (1×1) structure on SiC(0001).

After having confirmed the structure of our sample, we now investigate the non-equilibrium carrier dynamics triggered by photoexcitation with a visible pump pulse with a photon energy of $\hbar\omega_{pump} = 2$ eV and a fluence of $F = 0.3$ mJ/cm². Figure 2 shows trARPES snapshots of the graphene π -band at the K (Fig. 2a and b) and M-point (Fig. 2c and d) of the graphene Brillouin zone. The Sn-related bands could not be detected in the trARPES signal possibly due to a poor cross section at the photon energy used and/or the limited

signal-to-noise ratio.

Figure 2a shows a snapshot of the Dirac cone taken at negative pump-probe delay before the arrival of the pump pulse together with DFT calculations for free-standing graphene (orange lines). The corresponding pump-induced changes of the photocurrent at a pump-probe delay of $t = 80$ fs are shown in Fig. 2b. Gain and loss of photoelectrons with respect to negative delay are shown in orange and blue, respectively. We find a pronounced gain signal above the Fermi level, indicating a transient population of the conduction band up to energies of ~ 0.5 eV above the Fermi level. The valence band shows a loss that is strongest close to the Fermi level but reaches to much lower energies beyond the energy window covered in the experiment. The loss signal is accompanied by a pronounced gain below the equilibrium position of the Dirac cone, suggesting a transient down-shift of the dispersion. This is corroborated by the trARPES signal of the π -band at M in Figs. 2c and d, that show a snapshot at negative delay and the pump-induced changes of the photocurrent at a pump-probe delay of $t = 80$ fs, respectively. Just like Fig. 2b, Fig. 2d also shows a pronounced loss of photocurrent at the equilibrium position of the π -band and a gain below, consistent with a rigid down-shift of the π -band.

To analyze the pump-probe signal in greater detail, we first focus on the energy- and momentum-resolved non-equilibrium carrier dynamics (Fig. 3). Figure 3a shows the photocurrent, integrated over the areas marked by the colored boxes in Fig. 2b, as a function of pump-probe delay together with single-exponential fits. The resulting lifetime τ as a function of energy is shown in Fig. 3b. We find that the lifetime increases from $\tau \sim 70$ fs at $E = 0.5$ eV to $\tau \sim 400$ fs at $E = 0.1$ eV above the Fermi level. Figure 3c shows the transient carrier distribution inside the Dirac cone as a function of energy. The data points were obtained by integrating the trARPES snapshot over the momentum range indicated by the gray-shaded area in Fig. 2a. These carrier distributions were fitted with a Fermi-Dirac distribution convolved with a Gaussian to account for the finite energy resolution (gray line in Fig. 3c). The fitting range covers the gray-shaded area in Fig. 3c up to the Dirac point at $E_D = 35$ meV. The amplitude and the constant background of the Fermi fit were fixed to the value for negative pump-probe delays. We find that the carrier distribution at negative delay in the lower part of Fig. 3c is well described with a Fermi-Dirac distribution. At a pump-probe delay of $t = 80$ fs, however, we find clear deviations from a Fermi-Dirac distribution for energies above the Dirac point, indicating the presence of non-thermalized carriers

(NTCs). To quantify the number of NTCs we integrate the residual between Fermi-Dirac fit and experimental data (blue in Fig. 3c) over the energy interval from the Dirac point (located at $E_D \sim +35$ meV in the sample used for trARPES experiments) to $E = 0.84$ eV. The resulting data points are shown in Fig. 3d as a function of pump-probe delay together with a single-exponential fit with a lifetime of $\tau = 340 \pm 60$ fs.

Next, we turn towards the possible down-shift of the π -band suggested by the trARPES snapshots in Fig. 2. To extract the transient binding energy of the Dirac cone at the K-point of the graphene Brillouin zone we proceed as follows: We extract momentum distribution curves (MDCs) at constant energy from the trARPES snapshot in Fig. 2a, that we fit with a Lorentzian (an example is shown in Fig. 4a). The resulting peak position k as a function of energy E yields the dispersion relation of the Dirac cone $E(k)$ that we fit with a straight line. We repeat this procedure for all pump-probe delays, fix the slope of the linear fit to the average value for negative pump-probe delays ($\hbar v_F = 6.8$ eVÅ), and obtain the transient shift of the Dirac cone that is shown in Fig. 4b. The blue line in Fig. 4b represents a Gaussian fit that reproduces the fact that the peak shift seems to be symmetric about its minimum. We find a transient downshift of the Dirac cone of $\Delta E_K = -16 \pm 1$ meV with a Gaussian full width at half maximum of FWHM= 470 ± 30 fs. The transient binding energy of the π -band at the M-point is extracted as follows: We integrate the trARPES snapshot in Fig. 2c over the momentum range indicated by the gray-shaded area and fit the resulting energy distribution curve (EDC) with a Lorentzian peak and a Shirley background (see Fig. 4c). We then repeat this procedure for all other pump-probe delays. The temporal evolution of the change of the Lorentzian peak position is shown in Fig. 4d together with a Gaussian fit (blue line). We find a transient downshift of the π -band at M of $\Delta E_M = -15 \pm 2$ meV with a Gaussian full width at half maximum of FWHM= 450 ± 70 fs. The shifts of the π -band at K and M are the same within the error bars in terms of amplitude and lifetime, indicating a rigid down-shift of the whole π -band.

Our main observations can be summarized as follows: The Dirac cone of graphene exhibits energy-dependent population dynamics with lifetimes ranging from $\tau \sim 400$ fs at $E = 0.1$ eV to $\tau \sim 70$ fs at $E = 0.5$ eV. We find a non-thermal carrier distribution with a lifetime of $\tau \sim 400$ fs as well as a transient rigid downshift of the π -band by $\Delta E = -15$ meV for FWHM ~ 450 fs.

DISCUSSION

The energy-resolved lifetime $\tau(E)$ of a typical non-equilibrium carrier distribution in photo-doped graphene is usually found to increase when approaching the Fermi level [22–24]. This has been previously attributed to a phonon bottleneck for carrier relaxation. When the excess energy of the carriers with respect to the Fermi level $|E - E_F|$ becomes smaller than the phonon energy $\hbar\omega_{phonon}$, phonon emission is strongly suppressed resulting in long population lifetimes [25]. Based on previous work on graphene on H-terminated SiC(0001) [22], graphene on 2D Sn is expected to exhibit picosecond lifetimes close to the Fermi level. Instead, we observe surprisingly short relaxation times below 400 fs. This suggests that the photoexcited carriers inside the Dirac cone of graphene efficiently relax via states provided by the metallic Sn layer at the interface between graphene and SiC substrate. A similar acceleration of carrier relaxation due to the presence of a metallic substrate has been previously observed in Refs. [26, 27]. Finally, the Dirac point, where the density of states is zero, acts as another bottleneck for carrier relaxation in graphene [28]. Photoexcited carriers were found to accumulate above the Dirac point resulting in a non-thermal distribution of carriers [29–31] as also observed in the present case. The observed lifetime of the NTCs in graphene on 2D Sn matches the value of the population lifetime close to the Fermi level, suggesting that the decay of the NTCs is also dominated by states in 2D Sn.

We now discuss possible scenarios that might explain the observed rigid down-shift of the graphene π -band. The observed transient increase in binding energy suggests that the graphene layer becomes positively charged. The most likely origin of the extra holes in graphene is the 2D Sn layer. In order to test this hypothesis, we compute the band structure of the graphene - 2D Sn heterostructure with DFT. We chose the $(\sqrt{3} \times \sqrt{3})R30^\circ$ supercell sketched in Fig. 5a rather than the true $(6\sqrt{3} \times 6\sqrt{3})R30^\circ$ supercell to reduce the computational effort [32]. The corresponding Brillouin zone is sketched in Fig. 5b. In Fig. 5c we display the computed band structure. The color code reveals the orbital composition of the states. Sn S_1 , S_2 and S_3 states originating from Sn $(p_x + p_y)$ -, and p_z -orbitals are shown in green and blue, respectively. The graphene π -band is shown in orange. Despite the weak vdW coupling between graphene and 2D Sn we find pronounced deviations from a mere sum of the individual band structures. There is a strong hybridization between graphene and Sn

p_z -states at the Fermi level along the Γ K-direction close to the K-point of the Brillouin zone of the supercell. We find a pronounced band gap opening of $E_{gap} \sim 230$ meV in the Dirac cone and a simultaneous change of the orbital composition from Sn-like to graphene-like. In Fig. 5d we plot the corresponding electron density for the states marked by the pink and green dots in Fig. 5c. We find that, at the momentum where the band gap in the Dirac cone opens, the electron density is delocalized over both the graphene and the 2D Sn layer. This provides a natural channel for efficient ultrafast charge transfer between the two layers [33].

Based on these findings we propose two possible scenarios for the transient charging of the graphene layer. The first scenario involves a direct electronic transition exciting electrons from occupied states in the graphene Dirac cone into unoccupied Sn p_x - and p_y -states (red arrow in Fig. 5c). This excitation would leave the graphene layer positively charged and the 2D Sn layer negatively charged. In the second scenario, electronic excitations would mainly occur within the individual layers (gray arrows in Fig. 5c). Ultrafast hole transfer from 2D Sn to graphene could then occur via the charge transfer states in Fig. 5d. Further investigations are needed to decide which of the two scenarios is more likely or if a combination of the two scenarios applies.

SUMMARY

In summary, our results clearly indicate that — despite the weak vdW interaction between the individual layers — graphene - 2D Sn heterostructures exhibit new emerging electronic properties that cannot be described by the mere sum of the individual layers. Using ARPES and DFT we confirmed that Sn intercalated at the interface between epitaxial graphene and SiC(0001) substrate arranges into the well known metallic (1×1) structure. Using trARPES we have shown that the non-equilibrium carrier distribution established in the Dirac cone of graphene via photo-doping with visible pump pulses rapidly decays via states of the 2D Sn layer. We have further demonstrated that the graphene layer exhibits a transient charging with holes. Supported by DFT calculations that reveal a pronounced hybridization between the graphene Dirac cone and Sn p_z -states close to the Fermi level, we attribute this either to direct inter-layer photo-excitation, or intra-layer photo-excitation followed by ultrafast charge separation via charge transfer states, or a combination of both. Future calculations

of the absorption and charge transfer rates for the graphene/(1 × 1)Sn/SiC(0001) structure should clarify which of these scenarios is the most likely one.

Our results have important implications for the development of novel sensors, photodetectors, and solar cells with improved efficiency and faster response times. Further, the graphene - 2D Sn heterostructure might be promising for future applications as supercapacitors with high power density and fast charge/discharge cycles or for novel quantum computing technologies, where rapid manipulation and transfer of quantum states are essential.

ACKNOWLEDGMENTS

We thank Dr. Emile Rienks for support during the ARPES measurements at the BESSY II electron storage ring operated by the Helmholtz-Zentrum Berlin. This work received funding from the Deutsche Forschungsgemeinschaft (DFG) via the research unit FOR 5242 (project Nos. 449119662 and 449119662), the collaborative research center CRC 1277 (project No. 314695032), the Cluster of Excellence ‘CUI: Advanced Imaging of Matter’ - EXC 2056 - project ID 390715994, as well as from the European Union’s Horizon 2020 research and innovation program under Grant Agreement No. 851280-ERC-2019-STG and Graphene Core 3 project (Grant Agreement No. 881603).

* isabella.gierz@ur.de

- [1] A. K. Geim and I. V. Grigorieva, Van der Waals heterostructures, *Nature* **499**, 419 (2013), <https://www.nature.com/articles/nature12385>.
- [2] K. S. Novoselov, A. Mishchenko, A. Carvalho, and A. H. C. Neto, 2D materials and van der Waals heterostructures, *Science* **353**, aac9439 (2016), <https://www.science.org/doi/pdf/10.1126/science.aac9439>.
- [3] D. M. Kennes, M. Claassen, L. Xian, A. Georges, A. J. Millis, J. Hone, C. R. Dean, D. N. Basov, A. N. Pasupathy, and A. Rubio, Moiré heterostructures as a condensed-matter quantum simulator, *Nature Physics* **17**, 155 (2021), <https://www.nature.com/articles/s41567-020-01154-3>.
- [4] Y. Liu, N. O. Weiss, X. Duan, H.-C. Cheng, Y. Huang, and X. Duan, Van der Waals heterostructures and devices, *Nature Reviews Materials* **1**, 16042 (2016), <https://www.nature.com/articles/natrevmats201642>.
- [5] C. Jin, E. Y. Ma, O. Karni, E. C. Regan, F. Wang, and T. F. Heinz, Ultrafast dynamics in van der Waals heterostructures, *Nature Nanotechnology* **13**, 994 (2018), <https://www.nature.com/articles/s41565-018-0298-5>.
- [6] C. Riedl, C. Coletti, T. Iwasaki, A. A. Zakharov, and U. Starke, Quasi-Free-Standing Epitaxial Graphene on SiC Obtained by Hydrogen Intercalation, *Phys. Rev. Lett.* **103**, 246804 (2009), <https://journals.aps.org/prl/abstract/10.1103/PhysRevLett.103.246804>.
- [7] I. Gierz, T. Suzuki, R. T. Weitz, D. S. Lee, B. Krauss, C. Riedl, U. Starke, H. Höchst, J. H. Smet, C. R. Ast, and K. Kern, Electronic decoupling of an epitaxial graphene monolayer by gold intercalation, *Phys. Rev. B* **81**, 235408 (2010), <https://journals.aps.org/prb/abstract/10.1103/PhysRevB.81.235408>.
- [8] N. Briggs, B. Bersch, Y. Wang, J. Jiang, R. J. Koch, N. Nayir, K. Wang, M. Kolmer, W. Ko, A. D. L. F. Duran, S. Subramanian, C. Dong, J. Shallenberger, M. Fu, Q. Zou, Y.-W. Chuang, Z. Gai, A.-P. Li, A. Bostwick, C. Jozwiak, C.-Z. Chang, E. Rotenberg, J. Zhu, A. C. T. van Duin, V. Crespi, and J. A. Robinson, Atomically thin half-van der Waals metals enabled by confinement heteroepitaxy, *Nature Materials* **19**, 637 (2020), <https://www.nature.com/articles/s41563-020-0631-x>.

- [9] H. Kim, O. Dugerjav, A. Lkhagvasuren, and J. M. Seo, Charge neutrality of quasi-free-standing monolayer graphene induced by the intercalated Sn layer, *Journal of Physics D: Applied Physics* **49**, 135307 (2016), <https://iopscience.iop.org/article/10.1088/0022-3727/49/13/135307>.
- [10] S. Hayashi, A. Visikovskiy, T. Kajiwara, T. Iimori, T. Shirasawa, K. Nakastuji, T. Miyamachi, S. Nakashima, K. Yaji, K. Mase, F. Komori, and S. Tanaka, Triangular lattice atomic layer of Sn (1×1) at graphene/SiC(0001) interface, *Applied Physics Express* **11**, 015202 (2017), <https://iopscience.iop.org/article/10.7567/APEX.11.015202>.
- [11] A. Visikovskiy, S. Hayashi, T. Kajiwara, F. Komori, K. Yaji, and S. Tanaka, Computational study of heavy group IV elements (Ge, Sn, Pb) triangular lattice atomic layers on SiC(0001) surface, arXiv:1809.00829 (2018), <https://arxiv.org/abs/1809.00829>.
- [12] K. Yaji, A. Visikovskiy, T. Iimori, K. Kuroda, S. Hayashi, T. Kajiwara, S. Tanaka, F. Komori, and S. Shin, Coexistence of Two Types of Spin Splitting Originating from Different Symmetries, *Phys. Rev. Lett.* **122**, 126403 (2019), <https://journals.aps.org/prl/abstract/10.1103/PhysRevLett.122.126403>.
- [13] K. V. Emtsev, A. Bostwick, K. Horn, J. Jobst, G. L. Kellogg, L. Ley, J. L. McChesney, T. Ohta, S. A. Reshanov, J. Röhrl, E. Rotenberg, A. K. Schmid, D. Waldmann, H. B. Weber, and T. Seyller, Towards wafer-size graphene layers by atmospheric pressure graphitization of silicon carbide, *Nature Materials* **8**, 203 (2009), <https://www.nature.com/articles/nmat2382>.
- [14] A. Varykhalov, 1^2 -ARPES: The ultra-high-resolution photoemission station at the U112-PGM-2a- 1^2 beamline at BESSY II, *Journal of large-scale research facilities* **4**, A128 (2018), <https://jlsrf.org/index.php/lrf/article/view/99>.
- [15] G. Kresse and J. Hafner, Ab initio molecular dynamics for liquid metals, *Phys. Rev. B* **47**, 558 (1993), <https://journals.aps.org/prb/abstract/10.1103/PhysRevB.47.558>.
- [16] G. Kresse and J. Furthmüller, Efficiency of ab-initio total energy calculations for metals and semiconductors using a plane-wave basis set, *Computational Materials Science* **6**, 15 (1996), <https://www.sciencedirect.com/science/article/pii/0927025696000080>.
- [17] G. Kresse and J. Furthmüller, Efficient iterative schemes for ab initio total-energy calculations using a plane-wave basis set, *Phys. Rev. B* **54**, 11169 (1996), <https://journals.aps.org/prb/abstract/10.1103/PhysRevB.54.11169>.

- [18] J. P. Perdew, K. Burke, and M. Ernzerhof, Generalized Gradient Approximation Made Simple, *Phys. Rev. Lett.* **77**, 3865 (1996), <https://journals.aps.org/prl/abstract/10.1103/PhysRevLett.77.3865>.
- [19] P. E. Blöchl, Projector augmented-wave method, *Phys. Rev. B* **50**, 17953 (1994), <https://journals.aps.org/prb/abstract/10.1103/PhysRevB.50.17953>.
- [20] G. Kresse and D. Joubert, From ultrasoft pseudopotentials to the projector augmented-wave method, *Phys. Rev. B* **59**, 1758 (1999), <https://journals.aps.org/prb/abstract/10.1103/PhysRevB.59.1758>.
- [21] <https://dx.doi.org/10.17172/NOMAD/2024.04.06-1>.
- [22] I. Gierz, S. Link, U. Starke, and A. Cavalleri, Non-equilibrium Dirac carrier dynamics in graphene investigated with time- and angle-resolved photoemission spectroscopy, *Faraday Discuss.* **171**, 311 (2014), <https://pubs.rsc.org/en/content/articlelanding/2014/fd/c4fd00020j>.
- [23] I. Gierz, M. Mitrano, J. C. Petersen, C. Cacho, I. C. E. Turcu, E. Springate, A. Stöhr, A. Köhler, U. Starke, and A. Cavalleri, Population inversion in monolayer and bilayer graphene, *Journal of Physics: Condensed Matter* **27**, 164204 (2015), <https://iopscience.iop.org/article/10.1088/0953-8984/27/16/164204>.
- [24] J. C. Johannsen, S. Ulstrup, A. Crepaldi, F. Cilento, M. Zacchigna, J. A. Miwa, C. Cacho, R. T. Chapman, E. Springate, F. Fromm, C. Roidel, T. Seyller, P. D. C. King, F. Parmigiani, M. Grioni, and P. Hofmann, Tunable Carrier Multiplication and Cooling in Graphene, *Nano Letters* **15**, 326 (2015), <https://pubs.acs.org/doi/full/10.1021/nl503614v>.
- [25] M. Sentef, A. F. Kemper, B. Moritz, J. K. Freericks, Z.-X. Shen, and T. P. Devereaux, Examining Electron-Boson Coupling Using Time-Resolved Spectroscopy, *Phys. Rev. X* **3**, 041033 (2013), <https://journals.aps.org/prx/abstract/10.1103/PhysRevX.3.041033>.
- [26] S. Ulstrup, J. C. Johannsen, A. Crepaldi, F. Cilento, M. Zacchigna, C. Cacho, R. T. Chapman, E. Springate, F. Fromm, C. Roidel, T. Seyller, F. Parmigiani, M. Grioni, and P. Hofmann, Ultrafast electron dynamics in epitaxial graphene investigated with time- and angle-resolved photoemission spectroscopy, *Journal of Physics: Condensed Matter* **27**, 164206 (2015), <https://iopscience.iop.org/article/10.1088/0953-8984/27/16/164206>.
- [27] P. Majchrzak, K. Volckaert, A. G. Čabo, D. Biswas, M. Bianchi, S. K. Mahatha, M. Dendzik, F. Andreatta, S. S. Grønberg, I. Marković, J. M. Riley, J. C. Johannsen, D. Lizzit, L. Bignardi, S. Lizzit, C. Cacho, O. Alexander, D. Matselyukh, A. S. Wyatt, R. T. Chapman, E. Springate,

- J. V. Lauritsen, P. D. King, C. E. Sanders, J. A. Miwa, P. Hofmann, and S. Ulstrup, Spectroscopic view of ultrafast charge carrier dynamics in single- and bilayer transition metal dichalcogenide semiconductors, *Journal of Electron Spectroscopy and Related Phenomena* **250**, 147093 (2021), <https://www.sciencedirect.com/science/article/pii/S0368204821000475>.
- [28] T. Winzer, E. Malić, and A. Knorr, Microscopic mechanism for transient population inversion and optical gain in graphene, *Phys. Rev. B* **87**, 165413 (2013), <https://journals.aps.org/prb/abstract/10.1103/PhysRevB.87.165413>.
- [29] I. Gierz, J. C. Petersen, M. Mitrano, C. Cacho, I. C. E. Turcu, E. Springate, A. Stöhr, A. Köhler, U. Starke, and A. Cavalleri, Snapshots of non-equilibrium Dirac carrier distributions in graphene, *Nature Materials* **12**, 1119 (2013), <https://www.nature.com/articles/nmat3757>.
- [30] I. Gierz, F. Calegari, S. Aeschlimann, M. Chávez Cervantes, C. Cacho, R. T. Chapman, E. Springate, S. Link, U. Starke, C. R. Ast, and A. Cavalleri, Tracking Primary Thermalization Events in Graphene with Photoemission at Extreme Time Scales, *Phys. Rev. Lett.* **115**, 086803 (2015), <https://journals.aps.org/prl/abstract/10.1103/PhysRevLett.115.086803>.
- [31] I. Gierz, Probing carrier dynamics in photo-excited graphene with time-resolved ARPES, *Journal of Electron Spectroscopy and Related Phenomena* **219**, 53 (2017), sI: The electronic structure of 2D and layered materials, <https://www.sciencedirect.com/science/article/pii/S0368204816301657>.
- [32] A. Mattausch and O. Pankratov, Ab Initio Study of Graphene on SiC, *Phys. Rev. Lett.* **99**, 076802 (2007), <https://journals.aps.org/prl/abstract/10.1103/PhysRevLett.99.076802>.
- [33] N. Hofmann, L. Weigl, J. Gradl, N. Mishra, G. Orlandini, S. Forti, C. Coletti, S. Latini, L. Xian, A. Rubio, D. P. Paredes, R. P. Causin, S. Brem, E. Malic, and I. Gierz, Link between interlayer hybridization and ultrafast charge transfer in WS₂-graphene heterostructures, *2D Materials* **10**, 035025 (2023), <https://iopscience.iop.org/article/10.1088/2053-1583/acdaab>.

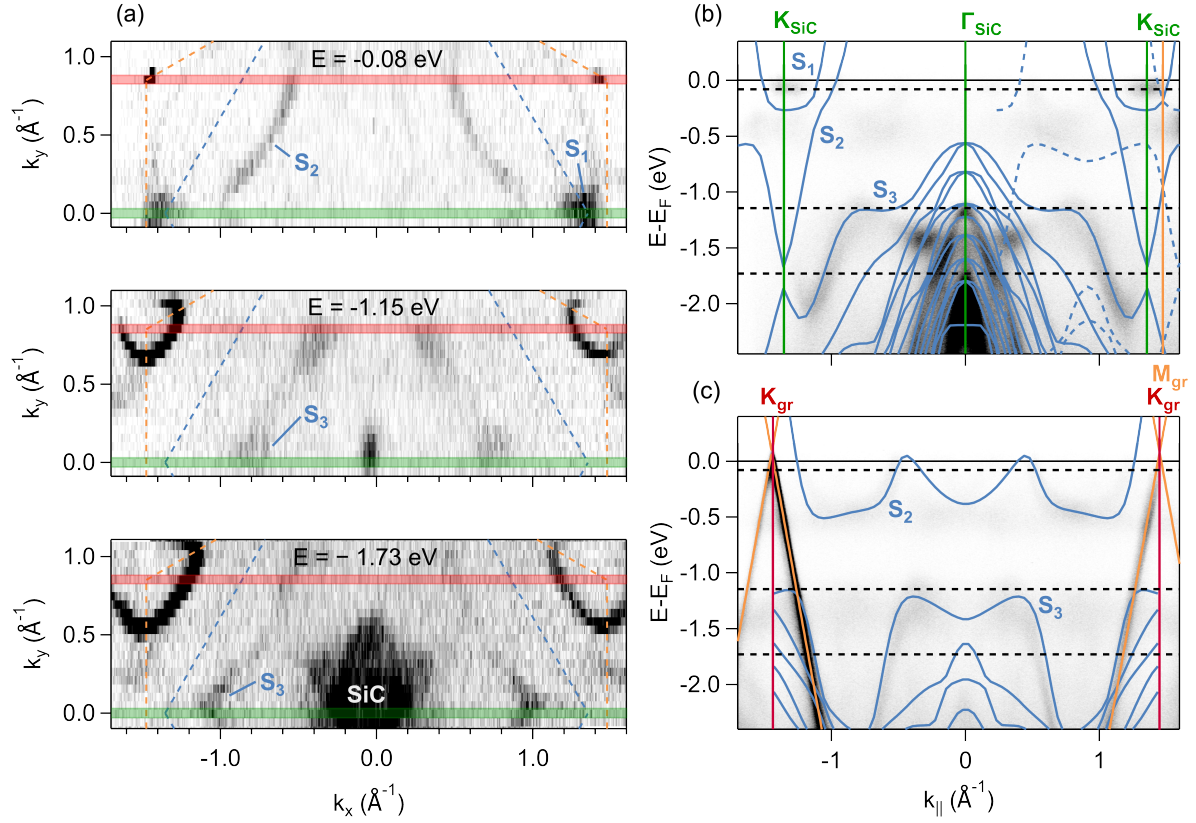


FIG. 1. **High-resolution ARPES of graphene - 2D Sn heterostructure.** (a) Photocurrent at constant energy as indicated in each panel. Dashed blue and oranges lines indicated the Brillouin zones of SiC(0001) and graphene, respectively. The three Sn-related states are marked in blue as S_1 , S_2 , and S_3 . Green and red lines indicate the directions along which the dispersion in panels (b) and (c), respectively, are plotted. (b) Band structure measured along the $K\Gamma K$ -direction of SiC(0001) together with DFT results of the (1×1) structure of Sn on SiC(0001) (blue lines). Dashed blue lines are Sn-bands that are backfolded at the M-point of graphene. (c) Band structure measured along the KK -direction of graphene together with DFT results of the (1×1) structure of Sn on SiC(0001) (blue lines) and free-standing graphene (orange lines). Dashed black lines in (b) and (c) indicate the energies of the constant energy contours in (a).

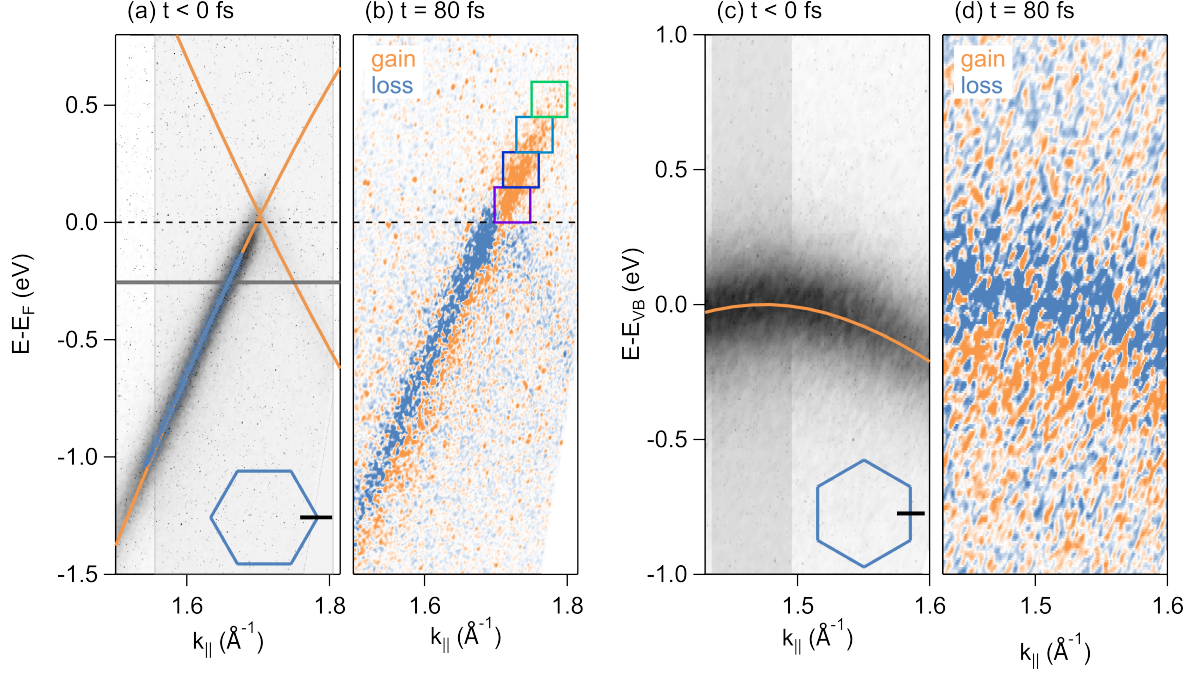


FIG. 2. **Time-resolved ARPES of graphene - 2D Sn heterostructure.** (a) Photocurrent along the ΓK -direction of graphene at the K-point of graphene (see Brillouin zone sketch in the inset) measured before the arrival of the pump pulse together with DFT calculations for freestanding graphene (orange lines). The thick gray line indicates the energy where the MDCs in Fig. 4a were extracted. The blue data points are the result of MDC fits in Fig. 4a. (b) Pump-induced changes of the photocurrent 80 fs after photo-excitation with a visible pump pulse with a photon energy of $\hbar\omega_{pump} = 2$ eV and a fluence of $F = 0.3$ mJ/cm². Orange and blue indicate a gain and loss, respectively, of photoelectrons with respect to negative pump-probe delay. Colored boxes indicate the areas of integration for the pump-probe traces presented in Fig. 3a. (c) and (d) are the same as (a) and (b) but measured at the M-point of graphene (see inset in c). The gray-shaded areas in (a) and (c) indicate the momentum range where the EDCs in Fig. 3c and Fig. 4c, respectively, were extracted.

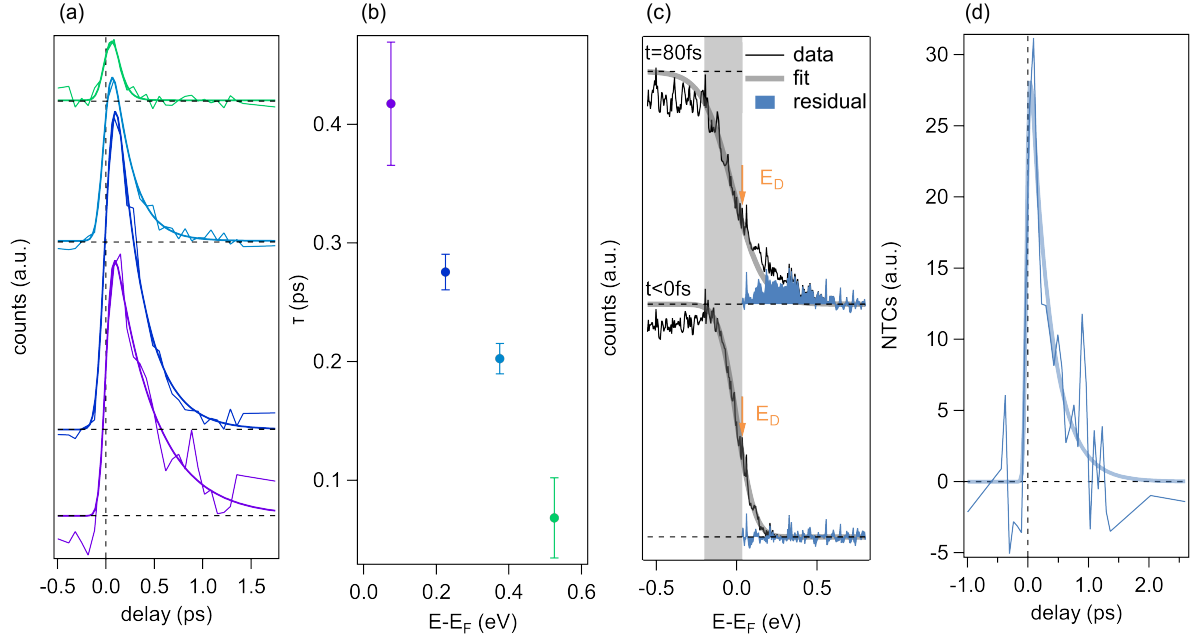


FIG. 3. Non-equilibrium population dynamics of graphene's Dirac cone (a) Photocurrent intergrated over the areas marked by the colored boxes in Fig. 2b as a function of pump-probe delay together with single-exponential fits. (b) Exponential lifetime τ extracted from the fits in panel (a) as a function of energy. (c) Distribution of electrons inside the Dirac cone of graphene obtained by integrating ARPES snapshots over the momentum range indicated by the gray-shaded area in Fig. 2a for two different pump-probe delays (thin black lines) as indicated. Thick gray lines are Fermi-Dirac fits. The position of the Dirac point (orange arrow) defines the upper energy of the fit range marked by the gray-shaded area. The blue-shaded area corresponds to the residual of the fit for energies above the Dirac point. (d) Number of non-thermalized carriers extracted from the size of the blue-shaded area in panel (c) as a function of pump-probe delay together with single-exponential fit with a lifetime of $\tau = 340 \pm 60$ fs.

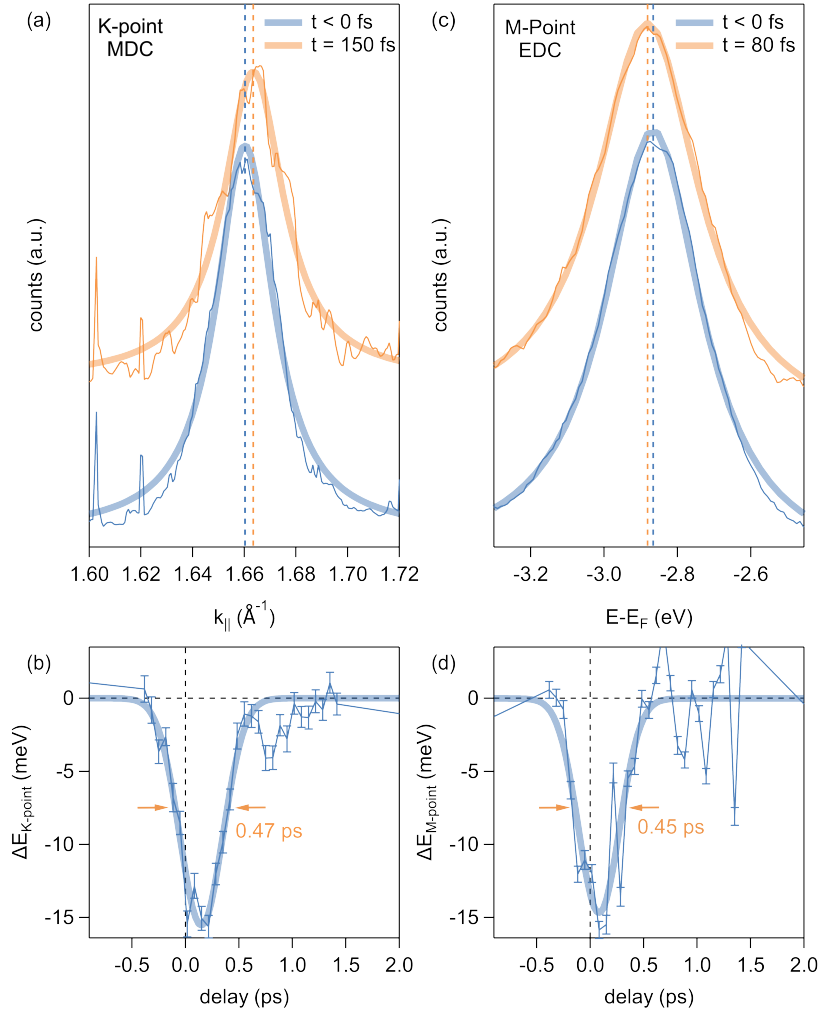


FIG. 4. **Transient shift of graphene π -band.** (a) MDCs extracted along the thick gray line in Fig. 1a for two different time delays together with Lorentzian fits. (b) Time-dependent peak shift of the Dirac cone from (a) together with Gaussian fit with a full width at half maximum of 470 ± 30 fs. The MDCs in (a) are offset for clarity. (c) Energy distribution curves obtained by integrating the ARPES snapshots at the M-point over the momentum range marked by the gray-shaded area in Fig. 2c together with Lorentzian fits for two different pump-probe delays. (d) Time-dependent peak position of the Lorentzian fits from (c) together with Gaussian fit with a full width at half maximum of 450 ± 70 fs.

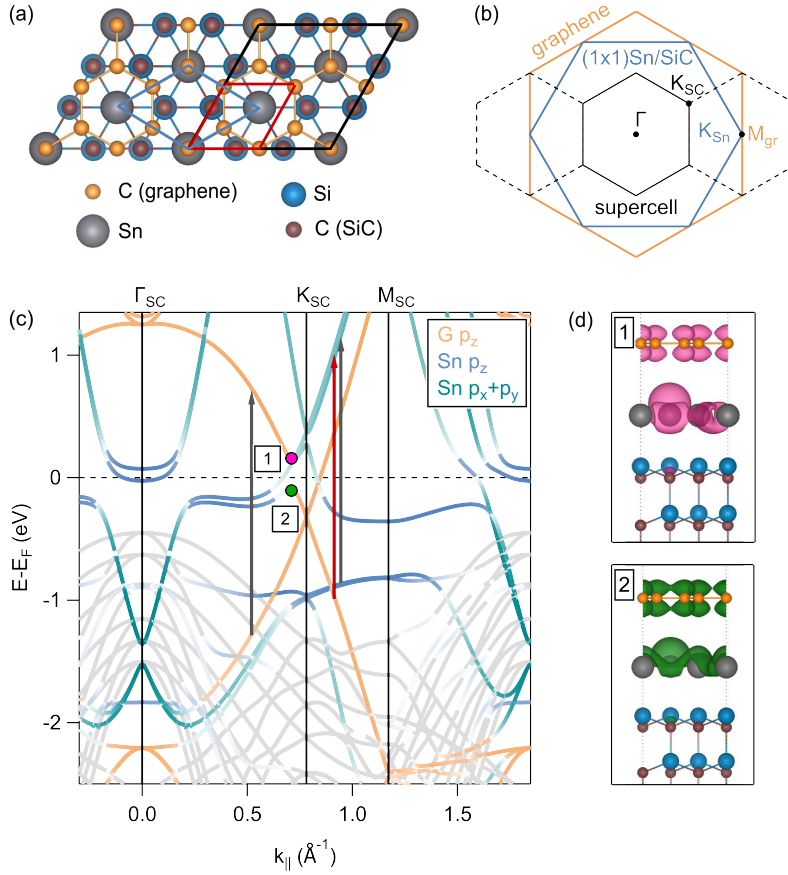


FIG. 5. DFT calculations for graphene - 2D Sn heterostructure. (a) Structural model with $(\sqrt{3} \times \sqrt{3})R30^\circ$ unit cell. (b) Sketch of the Brillouin zones of graphene (orange), $(1 \times 1)\text{Sn/SiC}(0001)$ (blue) and $(\sqrt{3} \times \sqrt{3})R30^\circ$ supercell (black). (c) Calculated band structure along $\Gamma K M \Gamma$ of the Brillouin zone of the $(\sqrt{3} \times \sqrt{3})R30^\circ$ supercell (SC). The color-code indicates the orbital composition of the states. Red and gray arrows indicate possible inter-layer and intra-layer transitions triggered by photo-excitation at $\hbar\omega_{pump} = 2 \text{ eV}$. The pink and green dots labeled 1 and 2 correspond to the location in the band structure $E(k)$ where the two electron densities shown in panel (d) were computed. (d) Absolute square of the wave function corresponding to the two eigenstates marked by pink and green dots in (c).